A Model of Effective Diffusion and Tortuosity in the Extracellular Space of the Brain

Jan Hrabe,* Sabina Hrabětová,† and Karel Segeth‡
*Center for Advanced Brain Imaging, Nathan S. Kline Institute, Orangeburg, New York; †Department of Physiology and Neuroscience, New York University School of Medicine, New York, New York; and ‡Mathematical Institute, Academy of Sciences of the Czech Republic, Prague, Czech Republic

ABSTRACT Tortuosity of the extracellular space describes hindrance posed to the diffusion process by a geometrically complex medium in comparison to an environment free of any obstacles. Calculating tortuosity in biologically relevant geometries is difficult. Yet this parameter has proved very important for many processes in the brain, ranging from ischemia and osmotic stress to delivery of nutrients and drugs. It is also significant for interpretation of the diffusion-weighted magnetic resonance data. We use a volume-averaging procedure to obtain a general expression for tortuosity in a complex environment. A simple approximation then leads to tortuosity estimates in a number of two-dimensional (2D) and three-dimensional (3D) geometries characterized by narrow pathways between the cellular elements. It also explains the counterintuitive fact of lower diffusion hindrance in a 3D environment. Comparison with Monte Carlo numerical simulations shows that the model gives reasonable tortuosity estimates for a number of regular and randomized 2D and 3D geometries. Importantly, it is shown that addition of dead-end pores increases tortuosity in proportion to the square root of enlarged total extracellular volume fraction. This conclusion is further supported by the previously described tortuosity decrease in ischemic brain slices where dead-end pores were partially occluded by large macromolecules introduced into the extracellular space.

INTRODUCTION

Diffusion is an important transport mechanism for many substances introduced into the extracellular space (ECS) of the brain. Macroscopic properties of this geometrically very complex environment can be summarized by two parameters, the ECS volume fraction α and its tortuosity λ (Nicholson, 2001). Volume fraction determines what percentage of the total tissue volume is accessible to the diffusing molecules. It is often called porosity in the porous media literature. Tortuosity describes the average hindrance of a complex medium relative to an obstacle-free medium.

Several methods exist, e.g., real-time iontophoresis (RTI) (Nicholson and Phillips, 1981) or integrative optical imaging (IOI) (Nicholson and Tao, 1993), for measuring these extracellular parameters both in brain slices and in live animals, and a wealth of experimental data has been accumulated over the last three decades. The findings are relevant for both healthy tissue and for many pathological states, e.g., ischemia, terminal anoxia, or brain trauma (Syková, 1997; Nicholson and Syková, 1998). The brain responds to most of these insults by lowering α below its typical value of ~0.2 (that is, 20%) and by increasing λ above the usual value of ~1.6 (Nicholson and Syková, 1998). Diffusion measurement can thus provide insight into the pathologies of these processes.

In addition, diffusion can serve as a probe into the local fine structure of the ECS geometry. Unfortunately, it has proved very challenging to establish any straightforward relationship between the microscopic properties of the ECS on one hand and the macroscopic and experimentally accessible parameters α and λ on the other hand. Even numerical solutions have mostly been limited to relatively simple two-dimensional (2D) arrangements (Chen and Nicholson, 2000). The principal difficulty is that although diffusion theory in complex media proved the existence of a unique tortuosity for any given geometry (Lehner, 1979), it has not provided any direct method to extract it. Consequently, it is also difficult to develop useful intuition for the effects of various local geometries.

To obtain a more explicit expression for geometric tortuosity, we will first extend Einstein's derivation of the integral formula for the diffusion coefficient (Einstein, 1956) by the addition of volume averaging. This step will accommodate very general and geometrically complex media. The effective diffusion coefficient becomes dependent on the diffusion time and on the average displacement probability for the individual molecules. With a simple approximation for the probability function, we can obtain effective diffusion coefficients in a number of 2D and three-dimensional (3D) geometries with small separations between the cellular elements. Despite its simplicity, the model shows good agreement with tortuosities obtained by Monte Carlo numerical simulations. It also offers an explanation for recent counterintuitive experimental findings (Patlak et al., 1998; Hrabětová and Nicholson, 2000; Hrabětová et al., 2003). These studies documented that an

Submitted December 31, 2003, and accepted for publication June 9, 2004.

Address reprint requests to Jan Hrabe, Center for Advanced Brain Imaging, Nathan S. Kline Institute, 140 Old Orangeburg Rd., Orangeburg, NY 10962. Tel.: 845-398-5471; Fax: 845-398-5472; E-mail: hrabe@mail.magalien.com.

0006-3495/04/09/1606/12 $2.00
doi: 10.1529/biophysj.103.039495

addition of large macromolecules into ECS makes the diffusion of a small marker molecule faster.

THEORY

Effective diffusion tensor, permeability, and tortuosity

Assume a macroscopically homogeneous (but not necessarily isotropic) environment composed of two phases, e.g., the cellular obstacles and the extracellular space occupying volume fraction α around them. We can define $\Phi(\vec{r},\vec{\delta})$ as the probability density for a diffusing particle in a position $\vec{r}=(x_1,x_2,x_3)$ inside the ECS at time t to be found in a position $\vec{r}+\vec{\delta}$ after some small fixed diffusion time τ. Particle motion is assumed to be restricted to the ECS during this time. In contrast to an obstacle-free environment, the probability depends on the initial position $\vec{r}$ and it is not necessarily symmetrical with respect to $\vec{\delta}$. We only assume that

$$\Phi(\vec{r}+\vec{\delta},-\vec{\delta})=\Phi(\vec{r},\vec{\delta}) \tag{1}$$

and that it is still normalized:

$$\iiint_{-\infty}^{\infty}\Phi(\vec{r},\vec{\delta})d\vec{\delta}=1. \tag{2}$$

Given the concentration $c(\vec{r},t)$ at time t and the above probability distribution, we would like to estimate concentration at time $t+\tau$. Following Einstein's argument (Einstein, 1956), this can be done by adding up all the particles that were in the right places at time t:

$$\begin{aligned}c(\vec{r},t+\tau)d\vec{r}&=d\vec{r}\iiint_{-\infty}^{\infty}c(\vec{r}+\vec{\delta},t)\Phi(\vec{r}+\vec{\delta},-\vec{\delta})d\vec{\delta}\\&=d\vec{r}\iiint_{-\infty}^{\infty}c(\vec{r}+\vec{\delta},t)\Phi(\vec{r},\vec{\delta})d\vec{\delta}.\end{aligned} \tag{3}$$

Using the Taylor expansions of $c(\vec{r},t)$ in time and spatial coordinates on the left-hand and right-hand side, respectively, we get

$$\begin{aligned}c(\vec{r},t)+\frac{\partial c(\vec{r},t)}{\partial t}\tau+\cdots=&\iiint_{-\infty}^{\infty}c(\vec{r},t)\Phi(\vec{r},\vec{\delta})d\vec{\delta}\\&+\iiint_{-\infty}^{\infty}\frac{\partial c(\vec{r},t)}{\partial x_i}\delta_i\Phi(\vec{r},\vec{\delta})d\vec{\delta}\\&+\iiint_{-\infty}^{\infty}\frac{\partial^2 c(\vec{r},t)}{\partial x_i\partial x_j}\frac{\delta_i\delta_j}{2}\Phi(\vec{r},\vec{\delta})d\vec{\delta}+\cdots,\end{aligned} \tag{4}$$

where we sum over spatial coordinate indices $i,j=1,2,3$. The expansions leave out second- and higher-order terms in time interval τ as well as third- and higher-order terms in $\vec{\delta}$. As noted by Einstein, this is possible if only small values of $\vec{\delta}$ contribute anything to the integral, which is in turn true if Φ differs significantly from zero only for small values of $\vec{\delta}$. Because local concentration does not depend on $\vec{\delta}$, the first terms on both sides cancel out as a consequence of probability normalization (Eq. 2). In an environment without obstacles, the second term on the right-hand side (representing an average displacement) will vanish because the probability is symmetrical with respect to δ_i. In a complex environment, however, this is not necessarily true. If the location $\vec{r}$ is close to an obstacle, the symmetry will clearly be violated.

We will now examine a sampling volume V_α of the ECS, sufficiently large to encompass the local geometrical variability, e.g., the ECS around several cellular elements. Consider spatial averages of all remaining terms of Eq. 4. The left-hand side yields simply a time derivative of the averaged concentration:

$$\begin{aligned}\frac{\tau}{V_\alpha}\iiint_{V_\alpha}\frac{\partial c(\vec{r},t)}{\partial t}d\vec{r}&=\frac{\partial}{\partial t}\left(\frac{\tau}{V_\alpha}\iiint_{V_\alpha}c(\vec{r},t)d\vec{r}\right)\\&=\frac{\partial\langle c(\vec{r},t)\rangle}{\partial t}\tau.\end{aligned}$$

In a macroscopically homogeneous environment the averaged probability does not depend on position $\vec{r}$ and it is always possible to select the sampling volume sufficiently large for $\langle\Phi(\vec{\delta})\rangle$ to become symmetrical with respect to displacement (so that $\langle\Phi(-\vec{\delta})\rangle=\langle\Phi(\vec{\delta})\rangle$). We can therefore employ the mean-value theorem and find a location $\vec{r}_1$ inside V_α such that

$$\begin{aligned}\frac{1}{V_\alpha}\iiint_{V_\alpha}\iiint_{-\infty}^{\infty}\frac{\partial c(\vec{r},t)}{\partial x_i}\delta_i\Phi(\vec{r},\vec{\delta})d\vec{\delta}\,d\vec{r}&\\=\frac{\partial c(\vec{r}_1,t)}{\partial x_i}\iiint_{-\infty}^{\infty}\delta_i\langle\Phi(\vec{\delta})\rangle d\vec{\delta}=0.&\end{aligned}$$

The only remaining term on the right-hand side of Eq. 4 can be treated similarly to find a location $\vec{r}_2$ inside V_α for which

$$\begin{aligned}\frac{1}{V_\alpha}\iiint_{V_\alpha}\iiint_{-\infty}^{\infty}\frac{\partial^2 c(\vec{r},t)}{\partial x_i\partial x_j}\frac{\delta_i\delta_j}{2}\Phi(\vec{r},\vec{\delta})d\vec{\delta}\,d\vec{r}&\\=\frac{\partial^2 c(\vec{r}_2,t)}{\partial x_i\partial x_j}\iiint_{-\infty}^{\infty}\frac{\delta_i\delta_j}{2}\langle\Phi(\vec{\delta})\rangle d\vec{\delta}.&\end{aligned}$$

Finally, if we assume that the second spatial derivative of concentration undergoes only negligible changes within the small volume V_α, the exact position of $\vec{r}_2$ representing the averaging volume becomes unimportant. We can then define a symmetrical tensor

$$D^*_{ij} = \frac{1}{\tau}\iiint_{-\infty}^{\infty} \frac{\delta_i \delta_j}{2} \langle \Phi(\vec{\delta}) \rangle d\vec{\delta} \tag{5}$$

and rewrite Eq. 4 as

$$\frac{\partial \langle c(\vec{r},t) \rangle}{\partial t} = D^*_{ij} \frac{\partial^2 \langle c(\vec{r},t) \rangle}{\partial x_i \partial x_j}, \tag{6}$$

where we again sum over $i, j = 1, 2, 3$. Clearly, this is the diffusion equation in a complex, anisotropic, and macroscopically homogeneous medium with the effective diffusion tensor D^*_{ij}. This result can also be arrived at (under similar assumptions) by an averaging process applied to the diffusion equation in a free environment with geometrically complex boundary conditions (Lehner, 1979). However, this approach does not lead to an explicit expression for the diffusion tensor.

Having both the microscopic and macroscopic diffusion equations, we can interpret the requirement that the second spatial derivative does not significantly vary within the averaging volume. If we express the concentration c as a sum of its mean value $\langle c \rangle$ and some fluctuation $\tilde{c}$, the second spatial derivatives of $\tilde{c}$ in the averaging volume should be negligible. This is equivalent to a requirement that

$$\frac{\partial \tilde{c}(\vec{r},t)}{\partial t} \ll \frac{\partial \langle c(\vec{r},t) \rangle}{\partial t}. \tag{7}$$

The macroscopic diffusion equation (Eq. 6), therefore, cannot describe phenomena with rapid concentration transients on a spatial scale of the averaging volume, which has to be large enough to capture the complexity of the environment. For example, the macroscopic brain ECS diffusion that assumes an averaging volume of several microns in diameter cannot be used to describe the diffusion of a neurotransmitter shortly after its release into a synaptic cleft.

In the case of a macroscopically isotropic and homogeneous environment, the probability Φ is radially symmetrical and the diffusion tensor is reduced to a scalar; Eq. 5 is simplified to

$$D^* = \frac{1}{3}\sum_{i=1}^{3} D^*_{ii} = \frac{1}{3\tau}\iiint_{-\infty}^{\infty} \frac{\delta^2}{2} \langle \Phi(\delta) \rangle d\vec{\delta}, \tag{8}$$

where $\delta = |\vec{\delta}|$. In a medium free of any obstacles, volume averaging can be performed over arbitrarily small volumes without violating any of the assumptions we have made, and the volume averages coincide with the local values. The definition of the diffusion coefficient in a one-dimensional (1D) case then becomes

$$D = \frac{1}{\tau}\int_{-\infty}^{\infty} \frac{\delta^2}{2} \Phi(\delta) d\delta, \tag{9}$$

which is the relationship given by Einstein (1956). The probability density $\Phi(\delta)$ in an n-dimensional case takes on the well-known Gaussian form with variance $\sigma^2 = 2nD\tau$:

$$\Phi(\delta) = \frac{1}{(4\pi n D\tau)^{\frac{n}{2}}} \exp\left(-\frac{\delta^2}{4nD\tau}\right). \tag{10}$$

Tortuosity λ is an auxiliary quantity related to the ratio of the effective and free diffusion coefficients. Various definitions exist, which may easily lead to confusion. In neurobiological applications, it is usually defined as

$$\lambda = \sqrt{\frac{D}{D^*}} \tag{11}$$

for a homogeneous and isotropic environment (Nicholson and Phillips, 1981; Nicholson, 2001). It is often interpreted as a path-length multiplication factor for molecules that have to find their way around obstacles. Although this idea works in a 1D environment (such as a tube) where the Laplace operator is reduced to a second derivative along a single axis, it breaks down in higher dimensions. The notion of diffusion ''path length'' loses meaning in higher dimensions. The relative contributions of all possible pathways would have to be taken into account. Despite its suggestive name, tortuosity does not have any straightforward relationship with the convoluted molecular circumnavigation of obstacles.

A more useful alternative for λ can be defined as

$$\theta = \frac{D^*}{D} = \frac{1}{\lambda^2} \tag{12}$$

with obvious generalization for the anisotropic case. The effect of θ is equivalent to a linear transformation of time in the diffusion equation, independently of the number of spatial dimensions. It can therefore be interpreted as a diffusion retardation factor caused by obstacles in the environment. The diffusion process in a geometrically complex environment is, in this sense, equivalent to a free diffusion process played out in a slow motion. We shall call θ a diffusion permeability. It can range from 0 for an entirely impenetrable medium ($\lambda = \infty$) to 1 for a medium free of any obstacles ($\lambda = 1$).

Note that other influences than a complex local geometry, e.g., a higher viscosity or a reversible uptake, may also act to slow down the diffusion. A diffusion experiment alone cannot distinguish between them.

Another point of potential confusion lies in alternative definitions of $c(\vec{r},t)$. If c_b is the amount of extracellular substance in a unit volume of the brain tissue (including both ECS and the cells), then the concentration in ECS is higher, $c = c_b/\alpha$. This is the concentration measured in the RTI experiments and referred to in Eq. 6. Other methods, such as

IOI, radiotracer method, or diffusion-weighted magnetic resonance (MR) spectroscopy of an extracellular marker, detect c_b instead.

It may seem that Eq. 8 can be used only when detailed knowledge of the probability distribution is available. It appears, however, that we can often make simple approximations to obtain useful results. As an example, consider the case of 1D diffusion restricted to a linear segment (a 1D ''box'') of length L. If the diffusion time τ is sufficiently long, the particle can be found with equal probability anywhere along the segment:

$$\Phi(x,\delta)=\begin{cases}\dfrac{1}{L} & \text{for } x\in\left\langle -\dfrac{L}{2},\dfrac{L}{2}\right\rangle, x+\delta\in\left\langle -\dfrac{L}{2},\dfrac{L}{2}\right\rangle \quad \text{and}\\ 0 & \text{elsewhere.}\end{cases}$$

Averaging over the segment length yields

$$\langle\Phi(\delta)\rangle=\begin{cases}\dfrac{L-|\delta|}{L^2} & \text{for } |\delta|<L \quad \text{and}\\ 0 & \text{elsewhere}\end{cases}$$

and therefore

$$D^*=\frac{2}{\tau}\int_0^L\frac{L-\delta}{L^2}\frac{\delta^2}{2}d\delta=\frac{L^2}{12\tau}, \tag{13}$$

which is in agreement with an asymptotic expression for the effective diffusion coefficient measured with diffusion-weighted MR (Callaghan, 1991). The apparent diffusion coefficient decreases with diffusion time as a result of the restriction on molecular movement. This situation is typical for intracellular substances that cannot escape into ECS.

We shall now turn to diffusion in the extracellular environment modeled by a system of uniform gaps between the cellular elements. We generally assume that the obstacles are closely packed together, leaving only narrow passages between them. This is almost always the case in the brain where the ECS volume fraction rarely exceeds 0.2. The diffusion in the interstitial gaps then represents essentially a 2D process in a 3D environment, or a 1D process in a 2D environment. The limits of the approximations in each case will be verified by numerical experiments described in the Results section.

2D environments

Squares

The simplest environment we consider is a periodic network of squares with uniform gaps between them. A unit element of this environment is formed by a single symmetrical cross of two perpendicular channels of side lengths $L_1 = L_2$ aligned with the x_1 and x_2 axes. The channels have identical width w. We assume that the gaps are narrow ($w \ll L_1$).

Because this environment is macroscopically homogeneous and isotropic, it is sufficient to examine diffusion in the unit element along one axis, e.g., the x_1 axis. Due to symmetrical arrangement at the channel crossings, the probability for a molecule in the L_1 channel to end up in the L_2 channel is the same as the probability of a transition in the opposite direction and we shall therefore assume that in the first approximation these channel transitions cancel out on the average. As a result, the diffusion looks the same as if the two perpendicular channels were independent of each other. The L_1 channel is then characterized by a free diffusion along the x_1 axis. We thus estimate (Einstein, 1956)

$$\Phi(\vec{r},\delta_1)=\begin{cases}\dfrac{1}{\sqrt{4\pi D\tau}}\exp\left(-\dfrac{\delta_1^2}{4D\tau}\right) & \text{for } \vec{r} \text{ inside the } L_1 \text{ channel, and}\\ 0 & \text{for } \vec{r} \text{ inside the } L_2 \text{ channel,}\end{cases}$$

which leads to a volume average over the unit element of the environment

$$\langle\Phi(\delta_1)\rangle=\frac{wL_1}{w(L_1+L_2)}\frac{1}{\sqrt{4\pi D\tau}}\exp\left(-\frac{\delta_1^2}{4D\tau}\right)$$

and therefore (see Eq. 8) to

$$D^*=\frac{1}{2}D, \quad \theta=\frac{1}{2} \quad \text{and} \quad \lambda=\sqrt{2}. \tag{14}$$

We expect the diffusion to slow down by a factor of 2 relative to the free environment.

Rectangles

In an anisotropic environment made of rectangles with $L_1 \neq L_2$, we similarly obtain effective diffusion coefficients along the x_1 and x_2 axes

$$D_{11}^*=\frac{L_1}{L_1+L_2}D \quad \text{and} \quad D_{22}^*=\frac{L_2}{L_1+L_2}D. \tag{15}$$

Random convex polygons

A model composed of random but tightly packed convex polygons with small gaps between them results in a macroscopically homogeneous and isotropic environment. The

sides of the polygons have random orientations with all directions being equally likely. We therefore need to average over all possible directions with uniform weighting.

When observing diffusion along the x_1 axis in a channel L running at an angle β_1 relative to x_1, the probability distribution $\phi(\vec{r})$ is simply compressed along x_1. The diffusion coefficient therefore appears to be reduced by a factor of $\cos^2\beta_1$ and averaging yields

$$\theta = \frac{1}{2\pi}\int_0^{2\pi}\cos^2\beta_1\, d\beta_1 = \frac{1}{2}. \tag{16}$$

As long as all the narrow channels are well connected (that is, there are no dead-end pores) and the environment is macroscopically homogeneous and isotropic, we would expect the same permeability and tortuosity as for the periodic network of squares. Another way to arrive at this conclusion is to realize that every channel of length L has the same effect as a union of its two independent projections to x_1 and x_2. Therefore, averaging all possible rectangles (Eq. 15), we again get

$$\theta = \frac{1}{2\pi}\int_0^{2\pi}\frac{|L\cos\beta_1|}{|L\sin\beta_1| + |L\cos\beta_1|}d\beta_1 = \frac{1}{2}. \tag{17}$$

Dead-end pores

Addition of dead-end pores significantly alters diffusion in a macroscopically homogeneous and isotropic environment such as the one composed of squares or random convex polygons. It does so by providing an extra space where molecules can be delayed. For sufficiently long diffusion times, the dead-end pores will act in a similar way as if extra channels were added in a direction perpendicular to the macroscopic diffusion flow. If we assume as before symmetry in the average probabilities for entering and leaving the dead-end pore, the permeability in a square lattice with added dead-end pores becomes

$$\theta = \frac{L_1}{2L_1 + L_p}, \tag{18}$$

where L_p is the combined length of the dead-end pores in the unit cell of the environment. In a randomized polygonal environment, L_1 and L_p would have to be replaced by their averaged values $\langle L_1\rangle$ and $\langle L_p\rangle$.

If we introduce the volume fraction of the well-connected space α_0 and the total volume fraction α into Eq. 18, an interesting relationship is revealed. Because of proportionalities $\alpha_0 \propto 2L_1$ and $\alpha \propto 2L_1 + L_p$, we get

$$\frac{\theta}{\theta_0} = \frac{2L_1}{2L_1 + L_p} = \frac{\alpha_0}{\alpha}, \quad \text{or} \quad \frac{\lambda}{\lambda_0} = \sqrt{\frac{\alpha}{\alpha_0}}, \tag{19}$$

where $\theta_0 = 1/2$ and $\lambda_0 = \sqrt{2}$ correspond to the environment lacking any dead-end pores (a well-connected environment). Therefore, in this approximation, adding well-connected space by making the gaps wider (within the $w \ll L_1$ limit) has negligible effect on permeability and tortuosity. On the other hand, adding dead-end space changes the hindrance according to the above relationship. The determining parameter is the ratio of the total ECS volume fraction to its well-connected part. We shall examine the limits of this highly simplified approximation in the Results section.

3D environments

Cubes

A periodic environment composed of closely spaced cubes with lengths $L_1 = L_2 = L_3$ along the x_1, x_2, and x_3 axes can be treated similarly to the squares in a 2D case. A unit element of the ECS environment is composed of three intersecting planes. Diffusion along any of the coordinate axes involves two planes aligned with the concentration gradient and one perpendicular to it. We therefore obtain average probability in this homogeneous and isotropic environment as

$$\langle\Phi(\delta_1)\rangle = \frac{w(L_1L_2 + L_1L_3)}{w(L_1L_2 + L_1L_3 + L_2L_3)}\frac{1}{\sqrt{4\pi D\tau}}\exp\left(-\frac{\delta_1^2}{4D\tau}\right) \tag{20}$$

and the effective diffusion coefficient, permeability and tortuosity are

$$D^* = \frac{2}{3}D, \quad \theta = \frac{2}{3} \text{ and } \lambda = \sqrt{\frac{3}{2}}. \tag{21}$$

It is interesting to note that the hindrance is lower than in the corresponding 2D case even though the path elongation around the cubes seems higher. It is another example that thinking in terms of pathways is misleading. It would be correct only for a 3D rectangular network of tubes where we would indeed obtain larger hindrance effect, $\theta = 1/3$, $\lambda = \sqrt{3}$ (Mathias, 1983).

Equations 20 and 21 provide another interpretation of diffusion permeability in the 3D environments composed of closely packed elements. The surface areas L_iL_j are proportional to the typical time to ''fill'' them during a 2D diffusion process for which $\langle L^2\rangle \propto 4D\tau$. We can consider these times as typical ''dwell'' times for the molecules diffusing along the corresponding planar elements. Although these times are mere approximations, the permeability involves only ratios of these quantities. We can therefore

consider a 1D macroscopic diffusion through the environment and express permeability as a ratio of dwell time ($\tau_{12} + \tau_{13}$) needed for diffusion with no perpendicular pathways (a process equivalent to the free diffusion), to the dwell time ($\tau_{12} + \tau_{13} + \tau_{23}$) consumed after the perpendicular planes are added. This approach leads to the same results and was described in more detail elsewhere (Hrabětová et al., 2003). It also agrees with the explanation of diffusion permeability as a time-delay factor.

Random convex polyhedra

The transition from a periodic environment of cubes to randomized polyhedra is analogous to the 2D procedure. Tightly packed convex polyhedra have sides in the shape of convex polygons with random orientations of normals. The environment is macroscopically homogeneous and isotropic.

When observing diffusion in a plane S with unit normal $(n_1, n_2, n_3) = (\cos\beta_1, \cos\beta_2, \cos\beta_3)$ from a viewpoint along the x_1 axis, it appears that the diffusion coefficient is reduced by a factor of $\cos^2\beta_2 + \cos^2\beta_3 = \sin^2\beta_1$. Averaging over all possible directions in space gives

$$\theta = \frac{1}{4\pi}\int_0^{2\pi}\int_0^{\pi} \sin^2\beta_1 \sin\beta_1 \, d\beta_1 \, d\phi = \frac{2}{3}. \qquad (22)$$

A random and well-connected 3D environment thus exhibits the same permeability as the periodic network of cubes. We could also treat the polygonal sides as a collection of its three independent projections and consider their respective average dwell times to obtain—thanks to macroscopic isotropy—the same result:

$$\theta = \frac{\langle\tau_{12}\rangle + \langle\tau_{13}\rangle}{\langle\tau_{12}\rangle + \langle\tau_{13}\rangle + \langle\tau_{23}\rangle} = \frac{\langle S_3\rangle + \langle S_2\rangle}{\langle S_3\rangle + \langle S_2\rangle + \langle S_1\rangle} = \frac{2}{3}. \qquad (23)$$

Dead-end pores

The most realistic and biologically relevant environment we consider is a 3D homogeneous and isotropic medium containing dead-end pores. We assume the pores to have approximately the same width as the well-connected channels and with openings that are small compared to the other dimensions of the unit cells. If the average volume of a dead-end pore in a unit cell of the environment is $\langle V_p\rangle$, the diffusion permeability is decreased in the same way as in the 2D case:

$$\theta = \frac{w(\langle S_3\rangle + \langle S_2\rangle)}{w(\langle S_3\rangle + \langle S_2\rangle + \langle S_1\rangle) + \langle V_p\rangle} = \frac{2w\langle S_1\rangle}{3w\langle S_1\rangle + \langle V_p\rangle}. \qquad (24)$$

Because $\alpha_0 \propto 3w\langle S_1\rangle$ (the well-connected ECS volume fraction) and $\alpha \propto 3w\langle S_1\rangle + \langle V_p\rangle$ (total ECS volume fraction), the Eq. 19 is still valid in 3D, even though the well-connected permeability changed to $\theta_0 = 2/3$ (and tortuosity to $\lambda_0 = \sqrt{3/2}$):

$$\frac{\theta}{\theta_0} = \frac{\alpha_0}{\alpha}, \quad \text{or} \quad \frac{\lambda}{\lambda_0} = \sqrt{\frac{\alpha}{\alpha_0}}. \qquad (25)$$

This equation can be used to estimate the amount of dead-end space in the brain tissue under various physiological conditions (Hrabětová and Nicholson, 2004).

METHODS

Numerical modeling

Geometrical models of complex environments were constructed as triangular meshes consisting of point coordinates and point connectivity data. Monte Carlo diffusion was simulated using the MCell program (Stiles and Bartol, 2001; Stiles et al., 2004) on various Linux workstations. Typically, 5000 molecules were released from a point source and allowed to diffuse for 1 s, divided into 10^6 time steps. For every molecule in every time step, the program determined the random displacement vector $\vec{\delta}$ from the probability distribution $\phi(\vec{\delta})$ valid for an obstacle-free 3D environment with diffusion coefficient $D = 10^{-6}$ cm^2/s. When the linear pathway intersected an obstacle representing a brain cell, it was simply reflected as if the collision was perfectly elastic.

To facilitate visual rendering by the OpenDX (www.opendx.org) script DReAMM (www.mcell.psc.edu), the MCell simulation generated a geometry file in a suitable format, together with 500 files containing molecule positions, typically creating one file every 2 ms of the diffusion time.

All 2D media were modeled essentially as very thin slabs (0.5 μm) of a 3D environment because there is no specific 2D module in the MCell program. Four point sources were spaced across this slab and enclosed by an impenetrable surface of a very narrow beam representing a line source ($0.05 \times 0.05 \times 0.5$ μm^3). The molecules were left to diffuse for 0.01 s inside the source beam to achieve initial distribution closely resembling a homogeneous line source. The source beam was then made transparent, releasing the molecules into the complex environment.

To estimate the permeability and tortuosity, we generalized the counting box approach used by Tao and Nicholson (2004). A counting box is invisible to the passing molecules and is only used to record the number of molecules inside it at prescribed time points. If the counting box dimensions along the x_1, x_2, and x_3 axes are a_1, a_2, and a_3, the box is expected to still contain

$$n(t) = n_0 \mathrm{erf}\left(\frac{a_1}{4\sqrt{D^* t}}\right)\mathrm{erf}\left(\frac{a_2}{4\sqrt{D^* t}}\right)\mathrm{erf}\left(\frac{a_3}{4\sqrt{D^* t}}\right) \qquad (26)$$

molecules out of the n_0 released at its center at time $t = 0$ (Crank, 1975). We recorded the counts at one hundred time points during the diffusion interval, using boxes of increasing size (typically 10 boxes with sizes 6, 12, . . . , 60 μm). The measured time dependencies were entered into a nonlinear fitting program implemented in IDL (Research Systems, Boulder, CO) to obtain the effective diffusion coefficient for every counting box. A median of these values was used as the best numerical estimate for the effective diffusion coefficient D^*, thus determining the diffusion permeability and tortuosity (Eq. 12).

Equation 26 was used for the 2D models as well, after setting $a_3 \to \infty$. Furthermore, it was also adapted to examine anisotropy in both the 2D and 3D environments, by simply letting two dimensions of the counting box

approach infinity and considering the diffusion along the single remaining dimension.

In a set of preliminary numerical experiments, two important assumptions were verified. First, a series of gradually decreasing time discretization steps was employed to find the maximum possible root mean square (RMS) displacement. It was found that a simulation interval 1 μs (corresponding to RMS displacement of $\sim$0.025 μm) was sufficiently small for all geometries with minimum gap widths of 0.1 μm. The only exception was the random 3D environment where we had to halve the RMS displacement. We used a gap width of at least 0.2 μm in the majority of experiments.

Second, given that any geometrical model has a finite size whereas at least some of the molecules will move very far, it is important to consider the effect of model boundaries. A combination of a small model with long diffusion time would necessarily distort the results. At the same time, the counting boxes (and of course the whole model as well) must contain sufficient number of cellular elements and the diffusion time has to be sufficiently long to reliably determine the effective diffusion. A typical size of the cellular elements in our geometries was 3 μm. The influence of the model size was tested by running the same experiment twice with two different boundary conditions. In one case the outer boundary was made reflective whereas in the other one it was made absorptive. From the observed differences of the two cases we found the maximum size of the counting box for which the model boundaries had only negligible effect. Larger counting boxes were discarded. No more than two out of ten boxes had to be discarded for model sizes 60–90 μm across and a diffusion time of 1 s.

Simple periodic geometries are straightforward to generate. The random polygonal models are more interesting. We employed Voronoi tessellations (Okabe et al., 2000) followed by a shrinkage of cellular elements, which gave rise to uniform gaps between them. First, pseudorandom seed points were generated on a rectangular grid in such a way that every cube (or square in the 2D case) of the grid ($3 \times 3 \times 3$ μm^3) contained exactly one seed point. The seed point was placed randomly inside a smaller concentric cube ($2.4 \times 2.4 \times 2.4$ μm^3). The point set was then processed by the Voronoi tessellation algorithm that produced a set of convex polyhedra (or polygons in the 2D case). Finally, the sides of these elements were parallel-shifted toward their center of gravity by half of the desired gap width. Any nonconvex cellular elements, arising due to complete elimination of some sides during this transformation, were detected and corrected. For the 2D random model, the algorithm was implemented in the IDL language but only the QHULL package (Barber et al., 1996) was able to deal reliably with the 3D case.

RESULTS

2D environments

The environment composed of periodic squares (periodicity 3 μm, gaps 0.215 μm) had ECS volume fraction $\alpha = 0.14$. It is less than a typical value in a living tissue but we chose to perform the 2D simulations with gaps (rather than volume fractions) similar to the 3D environments. A total of 30×30 squares were laid down. Effective diffusion was examined separately for x_1 and x_2 axes to verify the isotropy. Median permeabilities were $\theta_1 = 0.534$ and $\theta_2 = 0.534$ (and tortuosities $\lambda_1 = 1.369$ and $\lambda_2 = 1.368$). The environment thus appears to be isotropic, with results close to the predicted $\theta = 1/2$ ($\lambda = \sqrt{2}$). Fig. 1 documents the fitting procedure of Eq. 26 with $a_1 = 6, 12, \ldots, 48$ μm, $a_2 \rightarrow \infty$ and $a_3 \rightarrow \infty$.

With this simple geometry, we also tested the influence of the exact positioning of the counting boxes. The counting box walls normally coincided with the gaps between the square cells. When the boxes were expanded to run across the centers of the cellular elements, the results were very similar, e.g., $\theta_1 = 0.526$ and $\lambda_1 = 1.379$.

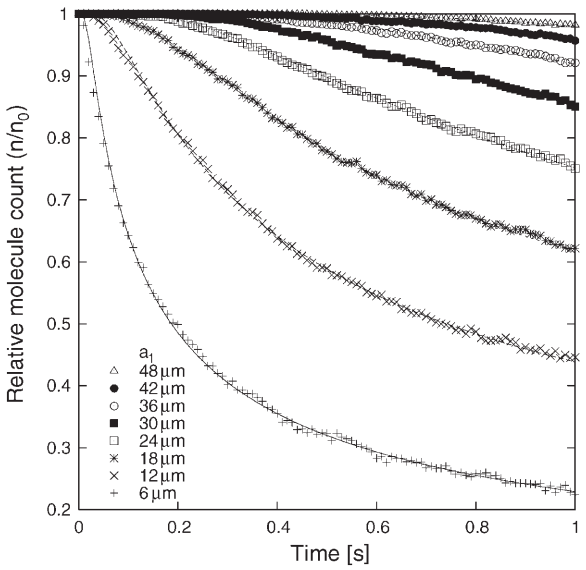

FIGURE 1 An example of the fitting procedure based on Eq. 26. Median effective diffusion coefficient was computed from fits corresponding to all individual counting boxes (eight in this case). This example shows fitting for effective diffusion along the x_1 axis in a 2D environment with square obstacles. To detect possible anisotropy, two sets of counting boxes were used, one with $a_2 \rightarrow \infty$ and the second one with $a_1 \rightarrow \infty$.

We examined only one anisotropic environment, created from rectangles with the side length ratio $L_1/L_2 = 2/1$. The gap width was the same as before (0.215 μm). The simulation resulted in $\theta_1/\theta_2 = 0.703/0.355 = 1.981$. Equation 15 predicts, in a good agreement, $\theta_1/\theta_2 = (2/3)/(1/3) = 2$.

A random 2D environment (Fig. 2) was generated by the procedure described in the paragraph on numerical modeling in the Methods section. There was one seed point (and therefore one cellular element) per 3×3 μm^2 of the surface. The gap was set uniformly to 0.2 μm. In agreement with Eq. 16, effective diffusion was very similar to the isotropic squares environment. We measured permeabilities $\theta_1 = 0.512$ and $\theta_2 = 0.519$ (corresponding to tortuosities $\lambda_1 = 1.397$ and $\lambda_2 = 1.388$).

The last series of 2D experiments (Fig. 3) served to examine the limits of the approximation given by Eq. 19 for the environment with dead-end pores. The dead-end pores were created as cul-de-sacs in all four sides of each element. The gap was kept 0.2 μm wide, both between the elements and in the pores. The amount of dead-end volume fraction ($\alpha - \alpha_0$) was varied exclusively by changing the depth of the pores (0.0,0.6, . . . , 2.4 μm). The results are summarized in Fig. 4 *A*. Similarly to the well-connected environment, the permeability is always slightly higher than predicted by the model, which assumes infinitely narrow gaps. Apart from

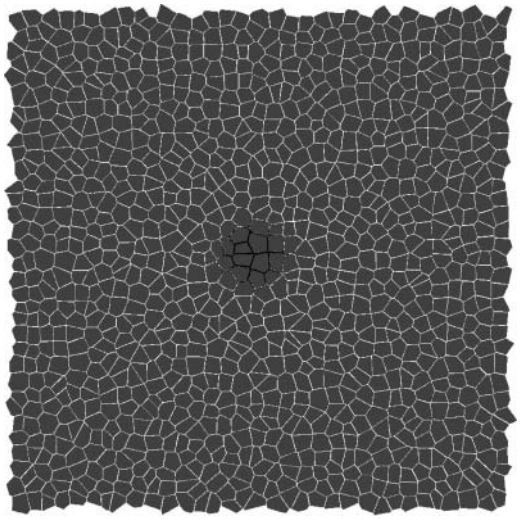

FIGURE 2 Geometrical arrangement of the 2D model composed of random polygons. Molecules are seen in black close to the release site. See text for details on modeling the 2D effective diffusion as a 3D process restricted to a thin layer.

this shift, the experimental results nicely follow the model prediction.

For lower values of α, we also tested different positions of the pores with respect to the square elements, placing them at the centers of the four sides. The differences were negligible. No anisotropy was detected in either case.

3D environments

The simplest 3D geometry was formed as a periodic network of cubes (period of 3 μm in each direction). We examined

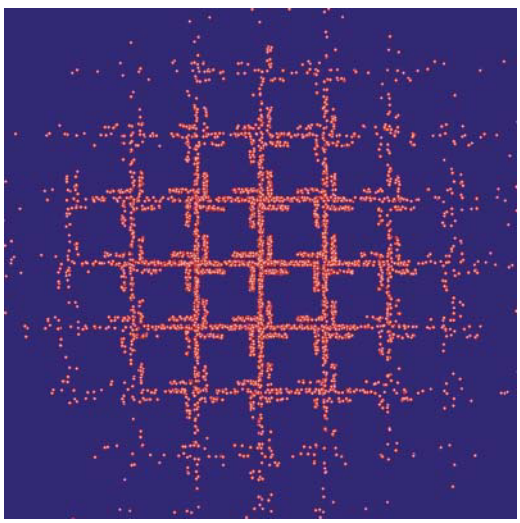

FIGURE 3 Dead-end pore diffusion. Cellular elements were removed to reveal the distribution of the diffusing molecules. The molecules are rendered as unrealistically large spheres to aid visualization. Because the molecules readily enter the dead-end pores, the effective diffusion observed on a macroscopic scale appears to be delayed. The elements are 3 μm across.

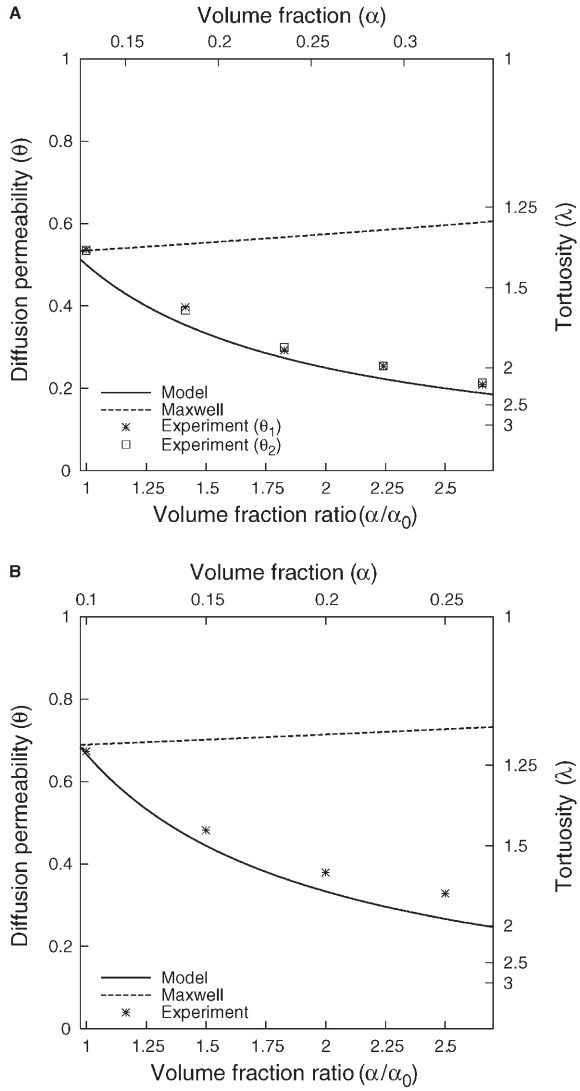

FIGURE 4 (*A*) 2D environment with pores. When dead-end volume fraction is added to the initial well-connected volume fraction α_0, the total ECS volume fraction α increases but the hindrance of the environment increases as well. This prediction is contained in Eq. 19 and confirmed by numerical simulations (data points for effective diffusion along both x_1 and x_2 axes are shown). In contrast, if α is increased by adding only well-connected space to α_0, the effective diffusion approximately follows Maxwell's curve with decreasing hindrance for higher volume fractions (Eq. 27a). The 2D model used $\alpha_0 = 0.129$. (*B*) 3D environment with pores. Dead-end pores added to the well-connected 3D environment increase the diffusion hindrance, as Eq. 25 predicts. Note that the mutual relationships are qualitatively similar to the 2D case (*A*) but all values are significantly shifted toward lower hindrance. This effect is characteristic of the transition to three dimensions. Addition of dead-end pores can lead to tortuosities commonly observed in the nervous tissue. The 3D model used $\alpha_0 = 0.1$ and the molecules were allowed to diffuse for 2 s, divided into 4×10^6 time steps.

ensembles of cubes with varying gap widths (0.1, 0.2, . . . , 0.6 μm), leading to varying ECS volumes α. Fig. 5 shows that the permeabilities are almost exactly predicted by the Maxwell homogenization theory ($\theta \approx 2/(3 - \alpha)$), originally derived for a suspension of loosely dispersed spheres

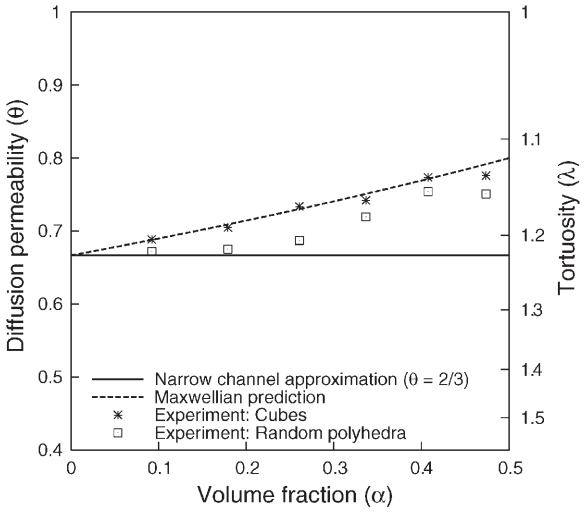

FIGURE 5 Decreasing the ECS volume fraction α by narrowing the channels between cellular elements decreases the tissue permeability only slightly. Both a simple model composed of cubes and a more realistic one with random convex polyhedra follow fairly closely Maxwell's homogenization estimate (Eq. 27b). The lowest achievable diffusion permeability is given by the narrow channel approximation (Eqs. 21 and 22). It is clear that manipulation of the uniformly wide and well-connected channels cannot account for experimental diffusion data in nervous tissue.

(Torquato, 2002), and, in analogy to the Clausius-Mossotti approximation for electric permeability, expected to be valid also for tighter arrangements of spheres. This confirms the result reported previously by Tao and Nicholson (2004). It is clear that for biologically relevant volume fractions of ~0.05–0.4, the permeabilities vary in a very small range, with the upper hindrance limit given by Eq. 21, which assumes narrow gaps.

We next examined whether this behavior could be replicated in a more realistic environment composed of random convex polyhedra (Fig. 6). The experiments confirmed validity of Eq. 22 for small α (Fig. 5). For larger ECS volume fractions, the effective diffusion is again very well described by the Maxwell relationship, even though the permeability is everywhere slightly lower than in the cubic environment. It is thus confirmed that the well-connected random geometries composed of convex elements produce permeabilities and tortuosities very similar to the periodic network of cubes. The narrow channel limit is an excellent approximation for most biologically relevant volume fractions. However, well-connected geometries cannot account for the higher diffusion hindrance measured in the central nervous system, be it healthy or under stress.

According to Eq. 25, adding dead-end pores to a well-connected ECS should increase the diffusion hindrance. We tested this assumption by adding pockets with openings in the sides of the cubic elements (Fig. 7). These modified cubes were randomly oriented. The results are summarized in Fig. 4 *B*. For the biologically interesting range of ECS volume fractions, Eq. 25 works quite well, even though the

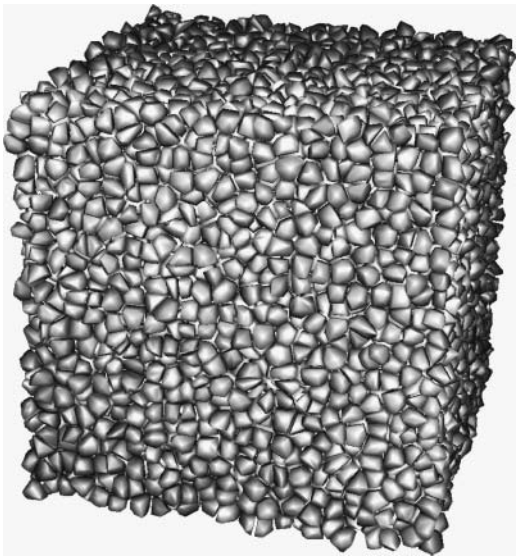

FIGURE 6 Illustration of the random 3D geometry composed of convex polyhedra. The gaps between the elements are uniform. Typical size of one cellular element is 3 μm. See text for more details on generating this model.

prediction becomes less accurate when the amount of dead-end space is larger. It is clear that dead-end pores could, in principle, account for the diffusion parameters in the nervous tissue. At the same time, the dramatic changes in effective diffusion during pathological insult could be explained by a change in the ratio of the dead-end volume fraction to the well-connected volume fraction.

In a separate set of experiments we verified the effects of the exact positioning and shape of the pockets. The differences between the arrangements with pockets close to

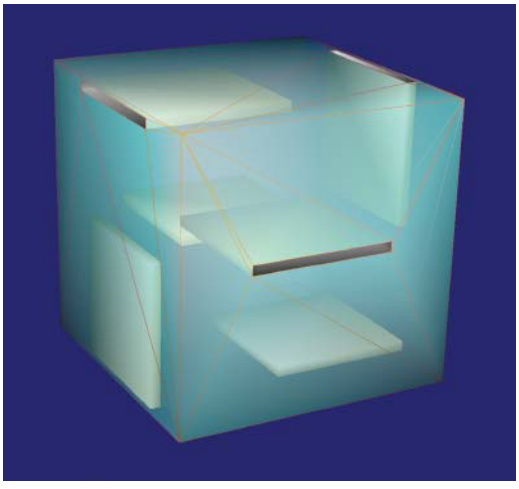

FIGURE 7 A single element of the 3D environment with dead-end pores. Pockets were made in every face of the cube, taking care to avoid mutual intersections while achieving maximum possible dead-end volume fraction. The orientation of each element in the environment was randomly selected from the 24 possible orientations. The width of the pore channels was identical to the gaps between the elements (0.104 μm).

the cube edges and near the side centers were negligible. Changes in the pocket shape had a larger effect. Shallower pockets with larger openings into the well-connected space (depth/length $\approx$ 1/2) departed from the model prediction more (8.1% error in tortuosity prediction for $\alpha = 0.16$) than deeper pockets with smaller openings (depth/length $\approx$ 2/1, 3.0% error in tortuosity prediction for $\alpha = 0.16$). This is expected because the model assumed that the openings are small relative to the size of the cubical elements. Square-shaped pockets used to generate Fig. 4 *B* differ from the model by ~4.6% in tortuosity.

DISCUSSION

Diffusion in a geometrically complicated environment is, on a microscopic level, an extremely complex process. Fortunately, in biological applications (as well as many others), we are often satisfied with macroscopic characterization. Remarkably, macroscopic diffusion in a complex environment can be described by the same diffusion equation as the diffusion in a free environment, except for a new and more general definition of the diffusion coefficient (Eq. 5).

Although there are other ways to derive the averaged diffusion equation (Eq. 6), we believe that the approach based on Einstein's original idea has several advantages. It is very straightforward and the origins of various assumptions that have to be made are easy to understand. It also leads to an explicit formula for the effective diffusion coefficient that ties it to the average displacement probability. Finally, it reveals the dependence of the effective diffusion on the diffusion time. In a free environment, the only requirement for the diffusion time τ is to be sufficiently long for the diffusing particle to ''forget'' its starting position. In contrast, different (and experimentally accessible) diffusion times in a complex environment can lead to very different results. This is easy to demonstrate experimentally by the diffusion-weighted-MR technique. Short diffusion times (e.g., several ms) emphasize properties of the immediate neighborhoods of the molecules at time $t = 0$ and the effective diffusion therefore resembles the free diffusion. With longer diffusion times (e.g., several tens of ms), more of the complex geometry is being explored and the effective diffusion becomes more in tune with the iontophoretic and IOI methods that normally utilize very long diffusion times (e.g., tens of seconds) (Nicholson and Phillips, 1981; Nicholson and Tao, 1993; Nicholson, 2001; Kroenke et al., 2003).

Unlike the porous media found in many nonbiological applications, the assemblies of brain cells develop in such a way that the cell walls yield to their neighbors and the spacing between the cells is comparatively uniform (van Harreveld, 1972). The geometry of this close packing is very different from a pile of sand or a sediment rock, for example. The ECS volume fraction in the brain is usually ~0.2, which means that the gaps between the cells are very narrow compared to the typical diameter of the cellular elements themselves. This structure, characteristic of nervous tissue, has made it possible to develop the narrow channel approximation. In this approximation, the exact width of the channels does not affect the effective diffusion, as long as it is small.

A complementary approach, starting from a diluted suspension of small spherical obstacles, is given by Maxwell's homogenization theory (Torquato, 2002). This point of view leads to permeability estimates

$$\theta = \frac{1}{2-\alpha} \quad \text{for a 2D environment, and} \tag{27a}$$

$$\theta = \frac{2}{3-\alpha} \quad \text{for a 3D environment.} \tag{27b}$$

Interestingly, in the limit of $\alpha \to 0$, these estimates happen to agree with our narrow channel approximation in the well-connected environment, even though Maxwell's assumptions are severely violated under these circumstances. This is probably the reason why Eqs. 27a and 27b work fairly well for a wide range of well-connected ECS volume fractions. However, the variations due to Eq. 27b are entirely outside of the range obtained experimentally both in normal and pathological nervous tissues. Some other factor limiting percolation must therefore be present. One possibility is the presence of the dead-end pores where diffusion can be delayed. Existence of dead-end pores gives the $\theta = \theta(\alpha)$ relationship an additional degree of freedom, thus making Eq. 27b inadequate for the description of nervous tissue. Enlarging the volume fraction can lead either to lower diffusion hindrance or to higher diffusion hindrance, depending on what exactly is enlarged—either the well-connected space or the dead-end space. The most important factor is the ratio of the well-connected and dead-end volume fractions. The total ECS volume has much smaller effect.

In pathological conditions such as hypoosmotic stress or ischemia, the cells swell and the ECS volume fraction is lowered (Nicholson and Syková, 1998). The dramatic increase in tissue hindrance commonly measured under these conditions is most likely attributed to the relative increase of the dead-end space (Hrabětová et al., 2003) because the hindrance becomes much higher than Eq. 27b would predict. This conclusion is corroborated by diffusion experiments with macromolecules. As shown by Hrabětová et al. (2003), adding the background macromolecules increases diffusion permeability (and decreases tortuosity), which cannot be easily explained without the presence of dead-end pores. The macromolecules are likely trapped in the dead-end pores and partly eliminate them, thus emphasizing the well-connected part of the ECS.

From the wealth of diffusion measurements in the brain and other nervous tissue we can estimate that ~40% of ECS

is located in the dead-end pores. This proportion is likely increased to ~60% under pathological stress (Hrabětová and Nicholson, 2004).

Our approach was strictly geometrical and any other effects, such as viscosity or reversible uptake, were neglected. Viscosity due to, e.g., extracellular matrix, could conceivably contribute to the observed diffusion hindrance. However, in the light of recent experiments in the ischemic brain slices (Patlak et al., 1998; Hrabětová et al., 2003), it seems increasingly unlikely that the viscosity contribution is large. Background macromolecules blocking the dead-end pores were able to lower the diffusion hindrance almost to its well-connected limit given by Eq. 22 (Patlak et al., 1998). This would not be possible if the ECS matrix played a significant role in hindering diffusion, unless the matrix is preferably distributed in the dead-end pores, for which there is no evidence. A similar argument can be made about the reversible uptake that would also lower the effective diffusion. Although there is not yet a definitive proof for the prominent role of the dead-end pores in the brain ECS, they appear to provide the most plausible explanation of the available data.

Electron micrographs lend some support for the existence of dead-end pores in the brain tissue. For example, the processes of glia, the most abundant cell type in the brain, possess a remarkable structural complexity that includes pocket-like formations (Špaček, 1985; Grosche et al., 1999). It is conceivable that more dead-end pores form in the ECS when gaps between the cells get occluded during ischemia or hypoosmotic stress. A study by van Harreveld and Malhotra (1967) shows many tight junctions between cellular elements in electron micrographs of ischemic neocortex.

Several limitations of the narrow channel models should be mentioned. First, it became clear that 2D models, even though they qualitatively have some features found in the brain diffusion, are characterized by consistently lower permeabilities (and higher tortuosities) than the 3D models. Their predictive value is therefore quite limited, except, of course, in the structures that are of approximately 2D nature, such as the nerve bundles. Although the 3D models are computationally much more demanding (on the order of days for a 1 s simulation run with 5000 molecules on a modern Linux PC), they should be employed whenever possible.

Second, geometries with larger volume fractions violate the narrow channel assumption. If the obstacles are convex and all of the ECS is well connected, the Maxwell model (Eq. 27b) may provide a better approximation. However, for biologically relevant values of α_0 (up to ~0.2), the difference between the Maxwell and the narrow channel models is small (up to 3.4% in tortuosity). In some geometries, notably the random polyhedra with $\alpha = \alpha_0 < 25\%$, the narrow channel estimate appeared better than the Maxwell approximation. Nonbiological applications with larger values of α_0 may benefit from an empirical correction to Eq. 25 based on a Maxwell relationship between θ_0 and α_0.

Finally, the accuracy of the narrow channel approximation with dead-end pores is lower for larger pore openings into the well-connected space. We have verified this effect by constructing an anisotropic environment that incorporated very shallow pockets with openings almost as wide as the cube sides ($\alpha_0 = 0.1$, $\alpha_d = \alpha - \alpha_0 = 0.09$). The pockets (similar to Fig. 7) were arranged so that four of them were aligned with the x_3 axis and four had openings perpendicular to the x_2 axis. The step randomizing the cube orientations was skipped. The tortuosity λ_2 (perpendicular to openings) was within 3.5% of the predicted value (1.8% with Maxwell empirical correction for λ_0). The diffusion along the pocket openings, however, was hindered much less than the model predicts. The error in λ_3 was ~17%. The reason is that this aligned arrangement effectively blurs the boundary between the well-connected space and the dead-end pore. The pore opening is so large that a portion of the pore close to the opening becomes indistinguishable from the well-connected space. This geometrical arrangement is artificial but it documents the least favorable case for the model application. In a macroscopically isotropic and homogeneous environment with parameters typical for a healthy brain ECS, we can estimate the errors in tortuosity due to finite widths of the well-connected gaps by ~1–2% (based on the Maxwell model) and the errors due to finite widths of pore openings by ~4–5% (based on randomly oriented square pockets). Both errors increase with larger volume fractions but in most pathological situations the volume fraction decreases below its physiological value, favoring the compliance with the model assumptions.

We have presented a derivation of the effective diffusion coefficient and shown how it can be estimated in a range of 2D and 3D models with narrow channels between tightly packed cellular elements. The geometrical model is presently able to explain the experimentally obtained diffusion properties in the nervous tissue in both physiological conditions and under pathological insults such as ischemia.

We gratefully acknowledge many exciting discussions with Professor C. Nicholson.

This work was in part supported by the National Institute of Neurological Disorders and Stroke of the National Institutes of Health (grant NS 28642 to C. Nicholson) and by the Grant Agency of the Czech Republic (grant 201-04-1503 to K. Segeth).

REFERENCES

Barber, C. B., D. P. Dobkin, and H. T. Huhdanpaa. 1996. The Quickhull algorithm for convex hulls. *ACM Trans. Math. Software*. 22:469–483.

Callaghan, P. T. 1991. Principles of Nuclear Magnetic Resonance Microscopy, 1st Ed. Clarendon Press, Oxford, UK.

Chen, K. C., and C. Nicholson. 2000. Changes in brain cell shape create residual extracellular space volume and explain tortuosity behavior during osmotic challenge. *Proc. Natl. Acad. Sci. USA*. 97:8306–8311.

Crank, J. 1975. The Mathematics of Diffusion, 2nd Ed. Oxford University Press, New York, NY.

Einstein, A. 1956. Investigations on the Theory of the Brownian Movement, 1st Ed. Dover, New York, NY.

Grosche, J., V. Matyash, T. Möller, A. Verkhratsky, A. Reichenbach, and H. Kettenmann. 1999. Microdomains for neuron-glia interaction: parallel fiber signaling to Bergmann glial cells. *Nat. Neurosci.* 2:139–143.

Hrabětová, S., J. Hrabe, and C. Nicholson. 2003. Dead-space microdomains hinder extracellular diffusion in rat neocortex during ischemia. *J. Neurosci.* 23:8351–8359.

Hrabětová, S., and C. Nicholson. 2000. Dextran decreases extracellular tortuosity in thick-slice ischemia model. *J. Cereb. Blood Flow Metab.* 20:1306–1310.

Hrabětová, S., and C. Nicholson. 2004. Contribution of dead-space microdomains to tortuosity of brain extracellular space. *Neurochem. Int.* 45:467–477.

Kroenke, C. D., J. J. Ackerman, and J. J. Neil. 2003. Magnetic resonance measurement of tetramethylammonium diffusion in rat brain: comparison of magnetic resonance and ionophoresis in vivo diffusion measurements. *Magn. Reson. Med.* 50:717–726.

Lehner, F. K. 1979. On the validity of Fick's law for transient diffusion through a porous medium. *Chem. Engin. Sci.* 34:821–825.

Mathias, R. T. 1983. Effect of tortuous extracellular pathways on resistance measurements. *Biophys. J.* 42:55–59.

Nicholson, C. 2001. Diffusion and related transport mechanisms in brain tissue. *Rep. Progr. Phys.* 64:815–884.

Nicholson, C., and J. M. Phillips. 1981. Ion diffusion modified by tortuosity and volume fraction in the extracellular microenvironment of the rat cerebellum. *J. Physiol.* 321:225–257.

Nicholson, C., and E. Syková. 1998. Extracellular space structure revealed by diffusion analysis. *Trends Neurosci.* 21:207–215.

Nicholson, C., and L. Tao. 1993. Hindered diffusion of high molecular weight compounds in brain extracellular microenvironment measured with integrative optical imaging. *Biophys. J.* 65:2277–2290.

Okabe, A., B. Boots, and K. Sugihara. 2000. Spatial Tessellations: Concepts and Applications of Voronoi Diagrams, 2nd Ed. Wiley, New York, NY.

Patlak, C. S., F. E. Hospod, S. D. Trowbridge, and G. C. Newman. 1998. Diffusion of radiotracers in normal and ischemic brain slices. *J. Cereb. Blood Flow Metab.* 18:776–802.

Špaček, J. 1985. Three-dimensional analysis of dendritic spines. III. Glial sheath. *Anat. Embryol. (Berl.).* 171:245–252.

Stiles, J. R., and T. M. Bartol. 2001. Monte Carlo methods for simulating realistic synaptic microphysiology using MCell. *In* Computational Neuroscience: Realistic Modeling for Experimentalists. E. De Schutter, editor. CRC Press, Boca Raton, FL.

Stiles, J. R., W. C. Ford, J. M. Pattillo, T. E. Deerinck, M. H. Ellisman, T. M. Bartol, and T. J. Sejnowski. 2004. Spatially realistic computational physiology: past, present, and future. *In* Parallel Computing: Software Technology, Algorithms, Architectures and Applications. G. Joubert, editor. Elsevier, Amsterdam, The Netherlands. In press.

Syková, E. 1997. The extracellular space in the CNS: its regulation, volume and geometry in normal and pathological neuronal function. *Neuroscientist.* 3:28–41.

Tao, L., and C. Nicholson. 2004. Maximum geometrical hindrance to diffusion in brain extracellular space surrounding uniformly spaced convex cells. *J. Theor. Biol.* 229:59–68.

Torquato, S. 2002. Random Heterogeneous Materials: Microstructure and Macroscopic Properties, 1st Ed. Springer-Verlag, New York, NY.

van Harreveld, A. 1972. The extracellular space in the vertebrate central nervous system. *In* The Structure and Function of Nervous Tissue. G. A. Bourne, editor. Academic Press, New York, NY.

van Harreveld, A., and S. K. Malhotra. 1967. Extracellular space in the cerebral cortex of the mouse. *J. Anat.* 101:197–207.